AGU PUBLICATIONS

Geochemistry, Geophysics, Geosystems

RESEARCH ARTICLE

10.1002/2015GC005858

Special Section:
Magnetism From Atomic to Planetary Scales: Physical Principles and Interdisciplinary Applications in Geo- and Planetary Sciences

Key Points:
- Maghemization of Fe_3O_4 grains is confirmed through XRD, Mossbauer, and EELS
- Maghemization of Fe_3O_4 grains occurs through formation of a core-shell structure
- Magnetic behavior is considered due to core-shell exchange coupling

Correspondence to:
T. P. Almeida,
t.almeida@imperial.ac.uk

Citation:
Almeida, T. P., A. R. Muxworthy, T. Kasama, W. Williams, C. Damsgaard, C. Frandsen, T. J. Pennycook, and R. E. Dunin-Borkowski (2015), Effect of maghemization on the magnetic properties of nonstoichiometric pseudo-single-domain magnetite particles, *Geochem. Geophys. Geosyst.*, *16*, 2969–2979, doi:10.1002/2015GC005858.

Received 9 APR 2015
Accepted 30 JUL 2015
Accepted article online 6 AUG 2015
Published online 12 SEP 2015

© 2015. The Authors.
This is an open access article under the terms of the Creative Commons Attribution License, which permits use, distribution and reproduction in any medium, provided the original work is properly cited.

Effect of maghemization on the magnetic properties of nonstoichiometric pseudo-single-domain magnetite particles

Trevor P. Almeida[1], Adrian R. Muxworthy[1], Takeshi Kasama[2], Wyn Williams[3], Christian Damsgaard[2,4], Cathrine Frandsen[4], Timothy J. Pennycook[5,6,7], and Rafal E. Dunin-Borkowski[8]

[1]Department of Earth Science and Engineering, Imperial College London, London, UK, [2]Center for Electron Nanoscopy, Technical University of Denmark, Kongens Lyngby, Denmark, [3]School of GeoSciences, University of Edinburgh, Edinburgh, UK, [4]Department of Physics, CINF, Technical University of Denmark, Kongens Lyngby, Denmark, [5]SuperSTEM Laboratory, Daresbury, UK, [6]Department of Materials, University of Oxford, Oxford, UK, [7]Now at Physics of Nanostructured Materials Group, Faculty of Physics, University of Vienna, Vienna, Austria, [8]Ernst Ruska-Centre for Microscopy and Spectroscopy with Electrons and Peter Grünberg Institute, Forschungszentrum Jülich, Jülich, Germany

Abstract The effect of maghemization on the magnetic properties of magnetite (Fe_3O_4) grains in the pseudo-single-domain (PSD) size range is investigated as a function of annealing temperature. X-ray diffraction and transmission electron microscopy confirm the precursor grains as Fe_3O_4 ranging from ~150 to ~250 nm in diameter, whilst Mössbauer spectrometry suggests the grains are initially near-stoichiometric. The Fe_3O_4 grains are heated to increasing reaction temperatures of 120–220°C to investigate their oxidation to maghemite (γ-Fe_2O_3). High-angle annular dark field imaging and localized electron-energy loss spectroscopy reveal slightly oxidized Fe_3O_4 grains, heated to 140°C, exhibit higher oxygen content at the surface. Off-axis electron holography allows for construction of magnetic induction maps of individual Fe_3O_4 and γ-Fe_2O_3 grains, revealing their PSD (vortex) nature, which is supported by magnetic hysteresis measurements, including first-order reversal curve analysis. The coercivity of the grains is shown to increase with reaction temperature up to 180°C, but subsequently decreases after heating above 200°C; this magnetic behavior is attributed to the growth of a γ-Fe_2O_3 shell with magnetic properties distinct from the Fe_3O_4 core. It is suggested there is exchange coupling between these separate components that results in a vortex state with reduced vorticity. Once fully oxidized to γ-Fe_2O_3, the domain states revert back to vortices with slightly reduced coercivity. It is argued that due to a core/shell coupling mechanism during maghemization, the directional magnetic information will still be correct; however, the intensity information will not be retained.

1. Introduction

During formation, magnetic minerals record the direction and intensity of the Earth's magnetic field. Paleomagnetists use this information to investigate, for example, past tectonic plate motion and geodynamo evolution. However, subsequent to formation, the constituent magnetic minerals are commonly exposed to a range of weathering conditions and environments. One of the most common weathering processes is maghemization, which is the oxidation of (titano)magnetite at ambient temperatures, i.e., the slow oxidation of (titano)magnetite to (titano)maghemite [*van Velzen and Zijderveld*, 1995]. Maghemization is known to be very common in mid-ocean ridge basalts >2 Ma [*Bleil and Petersen*, 1983; *Matzka et al.*, 2003], and understanding this general process is important as maghemization that is known to alter the original remanent magnetization [*Krása et al.*, 2005].

Of the constituent magnetic minerals, particles in the single domain (SD) grain size range (<100 nm) are regarded as ideal paleomagnetic recorders because of their strong remanence and high magnetic stability, with potential relaxation times greater than that of the age of the Universe [*Dunlop and Özdemir*, 2001]. However, magnetic signals from rocks are often dominated by small grains with nonuniform magnetization that exhibit magnetic recording fidelities similar to those of SD grains (termed pseudo-SD (PSD)).

In this paper, the progressive oxidation/maghemization of PSD magnetite (Fe_3O_4) to maghemite (γ-Fe_2O_3) is investigated. Oxidation of PSD Fe_3O_4 grains is a critical process of alteration of remanent magnetic signals and must be fully understood to allow for reliable interpretation of paleomagnetic data. The oxidation process starts at the Fe_3O_4 surface, where Fe^{2+} is either partially removed from the crystal or it reacts with

oxygen to form a new crystal layer [*O'Reilly*, 1984]. Further oxidation is driven by the oxidation gradient where Fe^{2+} diffuses from the interior of the grain to the surface, leaving vacancies in the interior. Hence, depending on the degree of oxidation, the Fe_3O_4 grains can be altered to structures ranging from a thin oxidized γ-Fe_2O_3 surface layer, a hetero-structured core-shell Fe_3O_4/γ-Fe_2O_3 grain or a fully oxidized γ-Fe_2O_3 grain.

Recent work using the transmission electron microscopy (TEM) technique of off-axis electron holography combined with environmental TEM visually showed a change in both strength and direction of remanent magnetization within PSD Fe_3O_4 particles, as a consequence of in situ oxidation within the TEM [*Almeida et al*., 2014]. This study is very important as it directly confirmed that oxidation can modify the original magnetic signal within individual Fe_3O_4 particles in the size range dominant in rocks. However, due to the reduced O_2 atmosphere pressures ($<$10 mbar) permitted for these in situ experiments, it was necessary to use elevated temperatures (800°C) to induce oxidation and hence is not directly representative of nature. Owing to the localized aspect of this study, it was limited to analysis of only a few individual PSD Fe_3O_4 particles and it is therefore perhaps incorrect to generalize this magnetic behavior to the larger numbers of grains within rocks. In this context, the ex situ oxidation of a bulk powder comprised entirely of PSD Fe_3O_4 grains, at comparatively lower temperatures, is reported. The chemical and structural transformation associated with low-temperature oxidation of the PSD Fe_3O_4 particles is related directly to their corresponding magnetic properties. This work is similar in objective to several previous studies [e.g., *Liu et al*., 2004; *Ge et al*., 2014]; however, unlike the previous studies, advanced TEM methods and Mössbauer spectroscopy, in addition to magnetic hysteresis and X-ray diffractometry (XRD), are applied.

2. Experimental

Synthetic Fe_3O_4 particles (diameter ranging from ~150 to ~250 nm) were purchased from Nanostructured and Amorphous Materials, USA. For heating experiments, discreet samples of 30 mg native Fe_3O_4 powder (Sample S1) were mixed with 20 ml ethanol in a beaker and dispersed using an ultrasonic bath. Dispersions were poured into a glass petri dish and then inserted into a temperature-controlled furnace at reaction temperatures of 120, 140, 160, 180, 200, and 220°C under ambient atmosphere (denoted as Samples S120–S220). To promote a uniform powder distribution, dispersions were heated until the ethanol had evaporated (~5 to 10 min), leaving a thin layer of powder, and subsequently heated for a further 2 h. After heating, the petri dish was removed and the dry reaction products were allowed to cool at room temperature.

The synthesized reaction products were deposited onto single crystal silicon substrates for crystallographic identification using XRD (PANalytical X'Pert PRO Diffractometer). For the purpose of TEM, the particles were dispersed in acetone using an ultrasonic bath before deposition onto lacey carbon/copper mesh support grids (Agar Scientific Ltd., UK). Conventional diffraction contrast imaging was performed using an FEI Titan TEM operated at 300 kV (Center for Electron Nanoscopy (CEN), Technical University of Denmark) and selected area electron diffraction (SAED) patterns allowed for phase identification. Electron-energy loss spectroscopy (EELS) analysis was performed at an energy resolution of ~0.3 eV, achieved through excitation of the monochromator, to provide information on sample oxidation state. High-angle annular dark field (HAADF) high-resolution scanning TEM (STEM) analysis was performed using a Nion UltraSTEM 100 at 100 kV (SuperSTEM, STFC Daresbury Laboratories, Daresbury, UK). EELS analysis was performed to measure the oxygen/Fe ratio and was quantified using Digital Micrograph software. The background signal was subtracted and, using the signal quantification parameters determined by the software, the relative area densities in the EEL spectra allowed the relative atomic ratios to be calculated. For the purpose of off-axis electron holography [*Dunin-Borkowski et al*., 1998], an FEI Titan with a C_S probe corrector on the condenser lens, equipped with a Lorentz lens and biprism, was used at 300 kV (CEN). Off-axis electron holograms were recorded in Lorentz mode with the objective lens switched off and the specimen in magnetic-field-free conditions at room temperature. Mean inner potential contributions to the recorded phase shift were removed by using in situ magnetization reversal [*Kasama et al*., 2011].

The magnetic measurements were conducted at the Natural Magnetism Group Laboratory at the Imperial College London and Technical University of Denmark. High-temperature thermomagnetic curves were measured using a Princeton Measurements vibrating sample magnetometer (VSM) fitted with a furnace

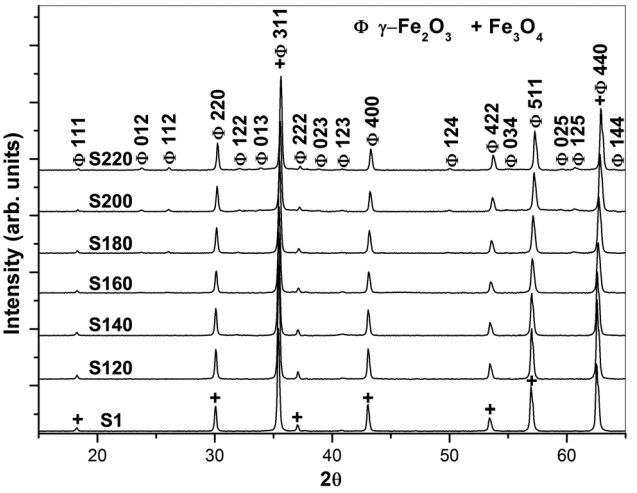

Figure 1. Room-temperature XRD patterns of Samples S1–S220 showing the effect of increasing temperature on the oxidation of Fe_3O_4 to γ-Fe_2O_3 (indexed, JCPDS 8-7119).

and heating was performed in flowing He. First-order reversal curve (FORC) diagrams and ^{57}Fe Mössbauer spectra were acquired from the reaction products at room temperature. The Mössbauer spectra are calibrated relative to α-Fe at room temperature.

3. Results

3.1. X-Ray Diffraction Analysis

The XRD patterns of Figure 1 illustrate the effect of increasing temperature on the crystallography of the reaction products. The peaks in the XRD pattern of Samples S1 are in good agreement with the presence of Fe_3O_4 (Joint Committee on Powder Diffraction standards (JCPDS) 75-449). Samples S120 and S140 exhibit XRD patterns similar to S1, whilst development of small peaks characteristic to γ-Fe_2O_3 (JCPDS 8-7119), can be seen with increasing reaction temperature in Samples S160–S220. The findings are in agreement with those of *Ge et al.* [2014] who made similar heating experiments for grains that were ~80 to 240 nm in diameter. In addition, the 2θ values were used to determine the interplanar lattice spacing (*d*) for the {220}, {311}, {400}, {511}, and {440} sets of lattice planes. The lattice parameter (*a*) was calculated from each set of (*hkl*) using the equation for the cubic crystal unit cell [*Cullity and Stock*, 2001], and the average was determined. The change in lattice parameter *a* as a function of reaction temperature is summarized in Table 1.

3.2. Transmission Electron Microscopy

Figure 2 provides information on the size, morphology, and crystallographic phase of the initial Fe_3O_4 precursor (Sample S1), along with the γ-Fe_2O_3 sample (S220), produced by heating to 220°C (Sample S220). The bright-field (BF) images of Sample S1 (Figure 2a) displays generally isotropic Fe_3O_4 grains (~150 to ~250 nm in diameter), as confirmed by SAED (Figure 2a, inset). EELS analysis of the O *1s K* edge, in the region 520–580 eV (Figure 2c), is indicative of Fe_3O_4 and composed of a prepeak (labeled a); a broad edge at higher energy (labeled b); along with higher-energy-loss structures, lying at about 548 eV (labeled c); and 563—565 eV (labeled d). Prepeak (a) results from the hybridization of Fe 3*d* and O 2*p* and usually splits into *t2g* and *eg* states by the ligand field. Peak (b) is composed of density of states from oxygen *p* character hybridized with metal 4*s* and 4*p* states [*Colliex et al.*, 1991]. The higher-energy-loss maxima in the fine structures (labeled c and d) are induced during the final state of the emitted electron, described as superposition, on the core-excited site, of an outgoing wave and of the multiple backscattered waves on the successive shells of neighboring oxygen ions [*Colliex et al.*, 1991]. EELS analysis of the Fe *2p* $L_{2,3}$ edge, in the region 704–726 eV (Figure 2d), confirmed the assignment of Fe_3O_4. The L_2 edge for this sample shows the typical shape of a mixed-valence compound, i.e., three visible features of differing intensities (Figure 2d, black arrows), whilst the almost shapeless L_3 edge is attributed to the combined spectral contributions of different iron sites (i.e., Fe^{2+} at octahedral B-sites and Fe^{3+} at both tetrahedral A and octahedral B-sites), consistent with the more delocalized structure of Fe_3O_4, as compared with other mixed iron oxides [*Crocombette et al.*, 1995; *Fujii et al.*, 1999].

Table 1. Lattice Parameter of the Unit Cell Determined From the XRD Patterns

Sample	Lattice Parameter *a* (Å)
S1	8.381
S120	8.373
S140	8.373
S160	8.365
S180	8.355
S200	8.342
S220	8.332

Figure 2b displays the γ-Fe_2O_3 grains formed after heating at 220°C for 2 h (Sample S220), as confirmed by SAED

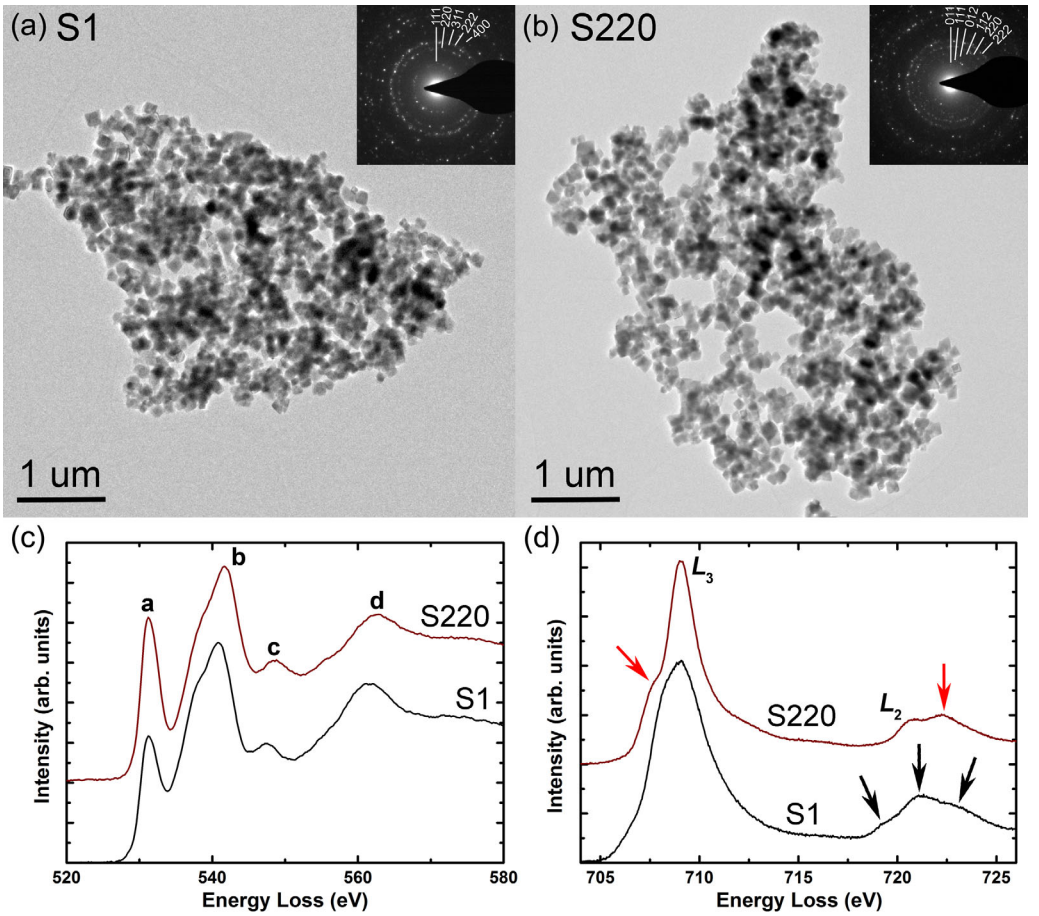

Figure 2. Room-temperature BF TEM images of precursor Fe_3O_4 particles (~150 to ~250 nm in diameter) (a) before (Sample S1); and (b) after heating to 220°C under an ambient air atmosphere (Sample S220), with associated SAED patterns inset, indexed to (a) Fe_3O_4 (JCPDS 75–449) and (b) γ-Fe_2O_3 (JCPDS 8–7119). Associated EEL spectra of the (c) O *K* and (d) Fe L_{23} edges, which were acquired in diffraction mode with signal emitted from all the Fe_3O_4 and γ-Fe_2O_3 particles in the field of view shown in the TEM images of Figures 2a and 2b.

(Figure 2b, inset). The alteration and development of fine features in the EEL spectra of Sample S220 are indicative of a change in the Fe oxidation state toward γ-Fe_2O_3 or α-Fe_2O_3 [*Chen et al*., 2004; *Gloter et al*., 2003; *van Aken and Lauterbach*, 2003]. An increase in the relative intensity of prepeak (a) in the O *1s K* edge with respect to the absorption maximum (b) (Figure 2c, Sample S220) is suggestive of oxidation to γ-Fe_2O_3. Similarly, it is recognized that development of a small prepeak in the L_3 edge and post-peak in the L_2 edge of the Fe *2p L* edge (Figure 2d, red arrows) are indicative of oxidation, with complete oxidation to γ-Fe_2O_3 being associated with a ~1.3 eV splitting in the L_3 edge [*Chen et al*., 2009].

The HAADF images of Figure 3 provide a closer examination of an individual Fe_3O_4 grain that was heated at 140°C (Sample S140). Figure 3a shows the grain to be rectangular in this projection, with approximate dimensions of ~130 nm long and ~110 nm wide. Higher magnification of the boxed region in Figure 3a is displayed in Figure 3b and highlights the characteristic lattice fringes of the {111} set of planes (inset). EEL spectra were acquired from the center, near-edge, and surface regions labeled A, B, and C, respectively, and the associated atomic weight composition (at %) was quantitatively determined from each cumulative EEL spectrum (summarized in Table 2). The data are suggestive of a slightly higher O content present at the surface of the nominally magnetite grain than at its near-edge and center.

Off-axis electron holography allowed for the imaging of the in-plane magnetization of Samples S1 and S220 and is presented in Figures 4 and 5. Figure 4a displays a BF TEM image of an individual native Fe_3O_4 grain (~180 nm in diameter) in Sample S1, where the corresponding magnetic induction map (Figure 4b) shows a magnetic vortex and stray magnetic field, revealing its PSD (vortex) nature. Similarly, the BF TEM image of

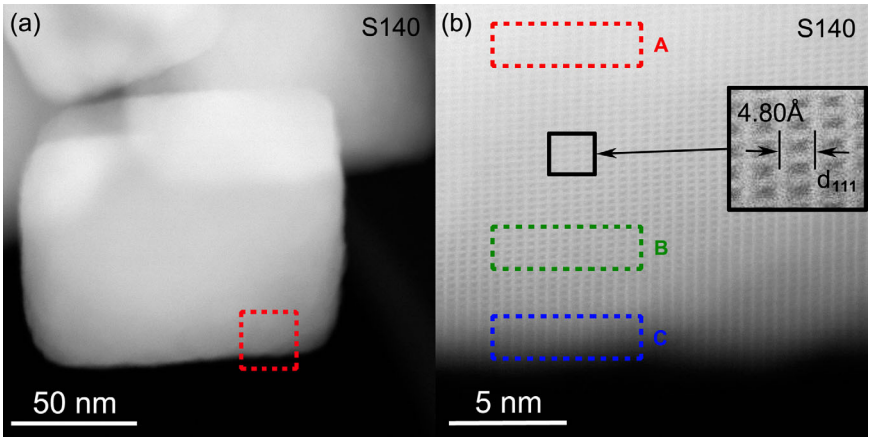

Figure 3. HAADF images of Fe_3O_4 particles heated to 140°C (Sample S140). (a) An individual rectangular Fe_3O_4 grain, 130 nm long and ~110 nm wide. (b) Magnification of the boxed region in Figure 3a, displaying characteristic lattice fringes of the {111} set of planes. EEL spectra were acquired from boxed regions labeled A, B, and C. Zone axis is <110>.

Figure 5a displays an individual γ-Fe_2O_3 grain (~200 nm in diameter) in Sample S220, where the corresponding magnetic induction map (Figure 5b) again reveals its PSD (vortex) nature.

3.3. Magnetic Properties

The Mössbauer spectra of Figure 6, acquired at room temperature, depict the transition from nonstoichiometric Fe_3O_4 to γ-Fe_2O_3 as a function of increasing reaction temperature. Mössbauer parameters were determined by fitting two sextets, St_1 (red) and St_2 (blue), with area ratios of the lines constrained to 3:2:1:1:2:3 for both sextets, using a Lorentzian fitting program called mfit (Table 3). The oxidation state from magnetite to maghemite of the samples was estimated as the magnetite content (wt %) in a magnetite-maghemite mixture, by considering the weighted average isomer shift δ_{aver} of the two sextets (Table 3) and using the linear relationship determined in *Da Costa et al.* [2014]:

$$\delta_{aver}\,(\mathrm{mm/s}) = 0.335 + 0.00215 * \mathrm{magnetite}\ \ (\mathrm{wt}\ \%)$$

The uncertainty of this model is estimated to about 5 wt % magnetite, given that δ_{aver} is determined with an error of 0.01 mm/s. The two sextets in the spectrum of S1 exhibit hyperfine parameters which at first may appear similar to pure Fe_3O_4, but the weighted average isomer shift of 0.46 mm/s (cf. $\delta_{aver} = 0.55$ mm/s for pure magnetite) and the relative spectral area of the two sextets of 0.93 (cf. $St_1/St_2 = 1.9$ for pure magnetite) [*Da Costa et al.*, 2014] suggest nonstoichiometric magnetite. Using the model of *Da Costa et al.* [2014], a magnetite content of 59% for Sample S1 is obtained. The spectra of Samples S120–S200 demonstrate further reduction in magnetite content and correspondingly oxidation to maghemite with increasing reaction temperature, as shown in Figure 7a and summarized in Table 3. Samples S200 and S220 display a typical spectrum of γ-Fe_2O_3, composed of two sextets with very similar hyperfine parameters [*Da Costa et al.*, 1995]. In addition, the oxidation parameter z was determined by comparing the F_B/F_A ratios in Table 3 to the average of the experimental data in *Ramdani et al.* [1987] and *Schmidbauer and Keller* [2006], where the oxidation parameter z varies from 0 to 1, representing a transformation from Fe_3O_4 ($z = 0$) to γ-Fe_2O_3 ($z = 1$) [*Readman and O'Reilly*, 1972; *Ge et al.*, 2014]. The relationship between the oxidation parameter z and the lattice parameter a is shown is Figure 7b, where z is shown to increase with the decreasing size of the cubic unit cell.

Table 2. Atomic Composition Calculated From Each Cumulative EEL Spectra Displayed as a Molar Ratio

	Element			
	O		Fe	
Spectrum	Atomic Ratio (O)	Content (at %)	Atomic Ratio (O)	Content (at %)
A	1.00 ± 0.00	55	0.82 ± 0.05	45
B	1.00 ± 0.00	55	0.82 ± 0.05	45
C	1.00 ± 0.00	57	0.75 ± 0.05	43

Figure 8 provides information on the effect of reaction temperature on the magnetic hysteresis of the

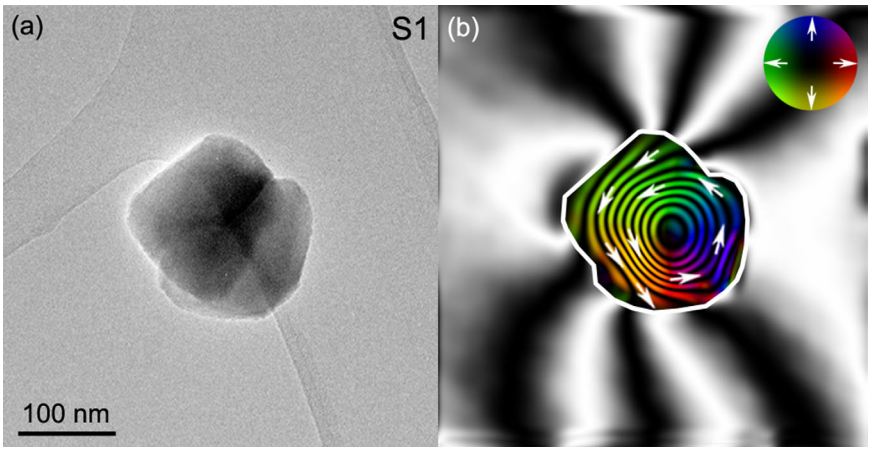

Figure 4. (a) BF TEM image of an individual native Fe_3O_4 particle (~180 nm in diameter, Sample S1); and (b) a magnetic induction map of the particle shown in Figure 4a. The magnetic contour spacing is 0.26 radians and magnetization direction is depicted in the color wheel.

reaction products and FORC diagrams of Samples S1 and S220. The coercivity (B_c) distribution in each sample is shown by horizontal profiles along the $B_u = 0$ axis of FORC data measured from Samples S1–S220 (Figure 8a). In addition, the measured values for coercivity of remanence (B_{cr}) and B_c are summarized in Table 4. A general trend of increasing B_{cr} values and B_c profiles with reaction temperature and oxidation can be seen up to 180°C, and exhibits a marked decrease thereafter, which is in agreement with the study of *Ge et al*. [2014]. The ratios of M_{rs}/M_s versus H_{cr}/H_c are plotted in Figure 8b (a "Day plot" [*Day et al*., 1977]) for the different reaction products. All the samples lie within the PSD region [*Dunlop*, 2002], however, Sample S220 plots distinctly toward the SD region, in agreement with the previous studies [*Liu et al*., 2004]. The FORC diagram of Sample S1 (Figure 8c) displayed PSD/SD type behavior with a distinct peak centered at a B_c value of ~22 mT [*Muxworthy and Dunlop*, 2002]. The peak in the FORC diagram of Sample S220 (Figure 8d) depicts similar behavior, but is centered at a lower B_c value of ~18 mT.

Curie temperatures (T_C) were determined using the second-derivative method [*Tauxe*, 1998] and the relationship with oxidation parameter z is presented in Figure 9a. Values of T_C were calculated as 583 ± 5°C for Samples S1 and S120, which is marginally above that of stoichiometric Fe_3O_4 [*Dunlop and Özdemir*, 2001]. The T_C of Samples S140 and S160 was slightly higher and a linear increase of T_C with temperature can be seen in Samples S180–S220, with a maximum T_C of 649 ± 5°C, which is in good agreement with that of γ-Fe_2O_3 [*Dunlop and Özdemir*, 2001]. This trend of increasing T_C with reaction temperature is similar to that seen in the oxidation process of titanomagnetites [*Readman and O'Reilly*, 1972]. The thermomagnetic curve of Sample S220 is presented in Figure 9b and the large difference between the heating and cooling curves

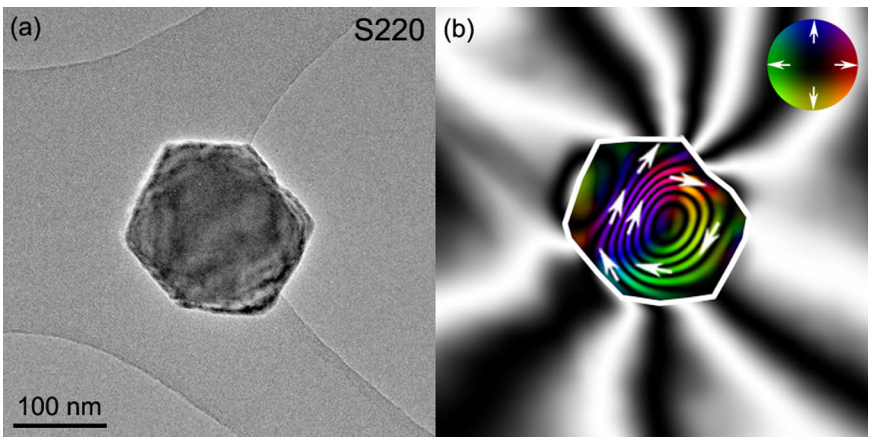

Figure 5. (a) BF TEM image of an individual γ-Fe_2O_3 particle (~200 nm in diameter, Sample S220); and (b) a magnetic induction map of the particle shown in Figure 5a. The magnetic contour spacing is 0.26 radians and magnetization direction is depicted in the color wheel.

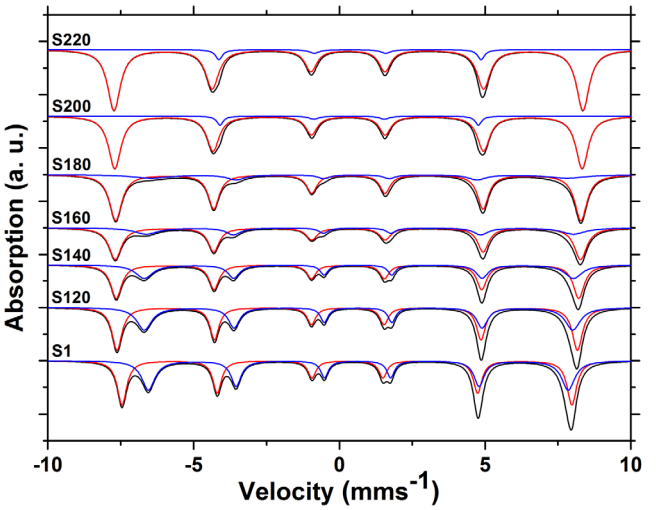

Figure 6. Mössbauer spectra of Samples S1–S220 (black) follow the maghemization of Fe_3O_4 as a function of reaction temperature. Mössbauer parameters were determined by fitting two sextets, St_1 (red) and St_2 (blue).

is indicative of possible inversion to hematite, which can be expected with heating of γ-Fe_2O_3 to elevated temperatures [*Özdemir and Dunlop*, 1988].

4. Discussion

4.1. Overview

This study has followed the maghemization of Fe_3O_4 grains in the PSD size range as a function of reaction temperature and the associated effect on their magnetic properties. The XRD pattern of Sample S1 is in good agreement of pure Fe_3O_4, which is reinforced by complementary SAED and characteristic O *1s K*/Fe *2p* $L_{2,3}$ edges in the associated EEL spectra. Further, TEM imaging showed the particles to be ~150 to ~250 nm in diameter and off-axis electron holography revealed their PSD nature. However, Mössbauer analysis of Sample S1 exhibited sextets with hyperfine parameters more indicative of nonstoichiometric Fe_3O_4, with an approximate composition of 59% magnetite and 41% maghemite. Increasing the reaction temperature led to the development of additional peaks in the XRD patterns of Samples S120–S200, and Sample S220 displayed an XRD pattern characteristic of γ-Fe_2O_3. This structural phase transformation is reinforced by the SAED pattern of Sample S220 and development of small peaks in the EEL spectra of Fe L_{23} edge further confirm the oxidation to γ-Fe_2O_3. TEM imaging shows the reaction products heated to 220°C retained their shape and without a marked change during the transition to γ-Fe_2O_3. Mössbauer spectra of Samples S120–S200 demonstrate a reduction in magnetite content and conversion to maghemite with increasing reaction temperature, where Sample S220 displays a typical spectrum of γ-Fe_2O_3 [*Da Costa et al.*, 1995; *Schmidbauer and Keller*, 2006].

4.2. Oxidation Mechanism

Oxidation of inverse spinel structured Fe_3O_4 under low-temperature conditions is known to involve topotactic transformation where the original morphology is maintained throughout [*Gallagher et al.*, 1968; *Cornell and Schwertmann*, 2003]. The reaction proceeds by outward migration of Fe^{2+} cations toward the surface of the crystal, thereby creating cation vacancies, and absorbed oxygen atoms at the surface oxidize the migrating cations to form a shell of γ-Fe_2O_3. In terms of diffusion pathways, when α-Fe_2O_3 is reduced to Fe_3O_4, the newly formed Fe_3O_4 {111} planes are parallel to the original α-Fe_2O_3 {006} planes, with the latter considered favorable planes for oxygen diffusion during thermal reduction [*Almeida et al.*, 2012]. Hence, in the reverse process of oxidation, the Fe^{2+} cations are suggested to preferentially diffuse along the Fe_3O_4 {111} planes,

Table 3. Mossbauer Parameters of Sextets St_1 and St_2 of Figure 6 Determined for Samples S1–S220[a]

	B_{hf} (T)		IS (mm s^{-1})		QS (mm s^{-1})		W (mm s^{-1})			Magnetite		
Sample	St_1	St_2	St_1	St_2	St_1	St_2	St_1	St_2	δ_{aver}	(wt %)	F_B/F_A	z
S1	47.9	44.7	0.28	0.65	−0.01	0.01	0.39	0.55	0.46	59	0.93	0.33
S120	49.0	45.6	0.29	0.66	−0.01	0.01	0.42	0.63	0.46	56	0.79	0.53
S140	49.3	45.7	0.30	0.67	−0.01	0.02	0.46	0.71	0.44	50	0.63	0.53
S160	49.6	45.5	0.32	0.67	−0.01	0.05	0.52	0.99	0.41	37	0.38	0.71
S180	49.5	44.3	0.32	0.65	0.00	0.04	0.51	1.62	0.39	25	0.23	0.85
S200	49.8	47.5	0.32	0.41	0.00	0.06	0.51		0.33	−0.55	0.13	0.96
S220	49.9	48.2	0.32	0.43	0.01	0.06	0.53		0.33	−1.9		0.99

[a] B_{hf} = magnetic hyperfine field, IS = isomer shift with regard to metallic Fe; QS = quadrupole splitting and W = line width of the outermost lines of a sextet (FWHM). δ_{aver} = weighted average isomer shift of sextets St_1 and St_2. Magnetite (wt %) calculated using the model of *Da Costa et al.* [2014]. F_B/F_A = relative area ratio of sextet B to sextet A. F_B/F_A is calculated assuming $\left[Fe_B^{2+}\right]\left[Fe_A^{3+}Fe_B^{3+}\right]$. The estimate for z was made by comparing F_B/F_A ratios to those in the literature [*Ramdani et al.*, 1987; *Schmidbauer and Keller*, 2006].

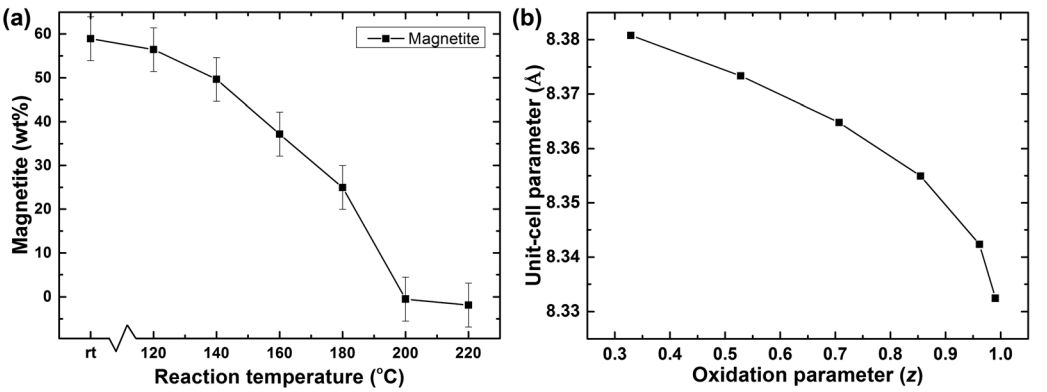

Figure 7. (a) Magnetite content in Samples S1–S220 as a function of increasing reaction temperature. (b) Relationship between the oxidation parameter z and the unit cell lattice parameter *a*.

with their relatively large lattice plane spacing of 4.79 Å providing a low energy diffusion pathway. For example, the HAADF image in Figure 3b shows the {111} planes to lie normal to the surface edge in the Fe_3O_4 grain and would provide an easy route for cation diffusion to the surface for oxidation. The fully oxidized inverse spinel structure of γ-Fe_2O_3 can be written as $Fe^{3+}\left[Fe\frac{3+}{5/3}\square_{1/3}\right]O\frac{2-}{4}$, where the octahedral sites are enclosed by the brackets and $\square$ denotes a lattice vacancy. The composition calculated quantitatively from the EEL spectra shows the surface of the Fe_3O_4 grain in Sample S140 (Spectrum C, Figure 3) to exhibit a slightly higher O content than toward its center. By implication, the observed lower surface Fe content provides evidence for the surface oxidation mechanism with the formation of core-shell Fe_3O_4/γ-Fe_2O_3 structures with increasing reaction temperature. However, the change in stoichiometry during oxidation of significantly larger Fe_3O_4 grains is considered to proceed more uniformly.

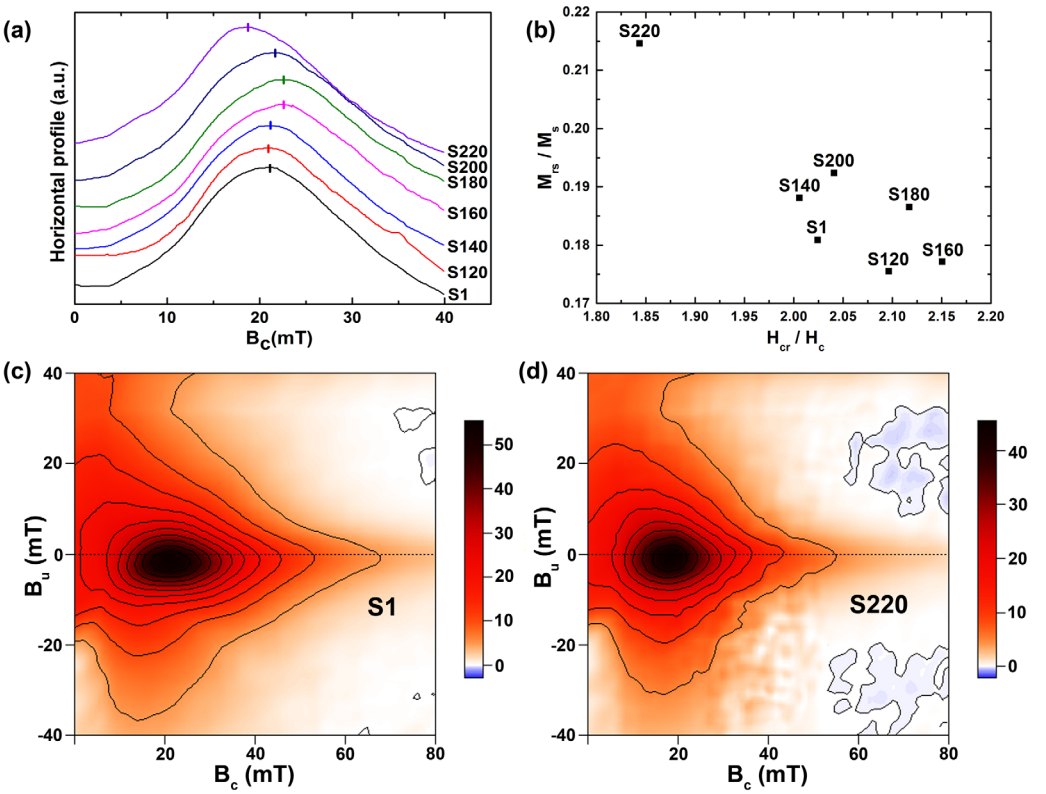

Figure 8. Magnetic properties of Samples S1–S220 as a function of increasing reaction temperature. (a) Graph of B_c profiles along the $B_u = 0$ axis extracted from the FORC diagrams, with the maximum value of the profile marked; and (b) a Day plot of the reaction products. (c, d) Normalized FORC diagrams of Samples (c) S1 and (d) S220, acquired at room temperature.

Table 4. Summary of Room-Temperature Hysteresis Parameters and Curie Temperatues of Samples S1–S220

Sample	B_c (mT)	B_{cr} (mT)	B_{cr}/B_c	M_s	M_{rs}/M_s	T_C (°C)
S1	12.37	25.04	2.02	0.47	0.18	583
S120	12.05	25.26	2.10	0.34	0.18	583
S140	12.35	24.77	2.01	0.26	0.19	589
S160	12.96	27.87	2.15	0.25	0.18	589
S180	13.33	28.22	2.12	0.14	0.19	608
S200	12.51	25.53	2.04	0.34	0.19	629
S220	12.21	22.51	1.84	0.23	0.21	649

4.3. Effect of Oxidation on Magnetic Properties

In Fe_3O_4, Fe^{2+} cations occupies the octahedral B-sites, whilst Fe^{3+} ions occupies both tetrahedral A and octahedral B-sites, and hence, the magnetic moments of the Fe^{3+} ions are mutually compensated and the net moment is attributed to the Fe^{2+} cations [*Mathew and Juang*, 2007]. In contrast, the ferrimagnetism of γ-Fe_2O_3 is the result of an average excess per formula weight $Fe_{8/3}O_4$ of $^2/_3$ of an Fe^{3+} ion on the B sublattice [*Dunlop and Özdemir*, 2001]. The T_C values for Samples S1 and S220 were indicative of Fe_3O_4 and γ-Fe_2O_3, respectively, whilst their FORC diagrams display PSD/SD type behavior with distinct peaks centered at ~22 and ~18 mT, respectively. Construction of magnetic induction maps from the off-axis electron holograms complemented the FORC data by visualizing the PSD domain state nature of both the Fe_3O_4 and γ-Fe_2O_3 grains. Interestingly, during the oxidation process from Fe_3O_4 to γ-Fe_2O_3, the B_c and B_{cr} values generally increased with reaction temperature up to 180°C, with subsequent decrease thereafter. *Ge et al.* [2014] reported a similar trend during oxidation of Fe_3O_4 particles in the PSD size range, which they interpreted using a micromagnetic numerical model: for PSD grains near the critical SD grain size boundary, as the Fe^{2+} cations diffuse toward the surface of the particle and the γ-Fe_2O_3 shell thickness increases through oxidation, the diameter of the Fe_3O_4 core decreases as a consequence. As the Fe_3O_4 core becomes smaller, the overall magnetic strength of the grain decreases due to the lower M_s of the γ-Fe_2O_3 skin, whilst exchange coupling of the Fe_3O_4 core to the γ-Fe_2O_3 skin maintains the high magnetocrystalline anisotropy, and at a point, the minimum energy domain structure is more SD-like. As oxidation proceeds the small Fe_3O_4 core shrinks sufficiently so that it is unable to provide a significant influence on the B_c, which collapses markedly as the grain reverts to a vortex structure. For larger PSD grains, the grains remain in a vortex state throughout the oxidation process, but vorticity of the magnetic domain state reduces as the γ-Fe_2O_3 skin grows. The magnetically harder and slightly more uniform domain structures result in a trend of increasing B_c until the Fe_3O_4 core almost disappears when both parameters decrease significantly, which is consistent with the experimental data and supports the proposed mechanism of maghemization proceeding through the formation of core-shell Fe_3O_4/γ-Fe_2O_3 structures. Due to the rather subtle changes observed in the B_c values and FORC diagrams, the transition from vortex state to vortex with reduced vorticity is considered to be the dominant mechanism in this study. It appears unlikely given the small increases

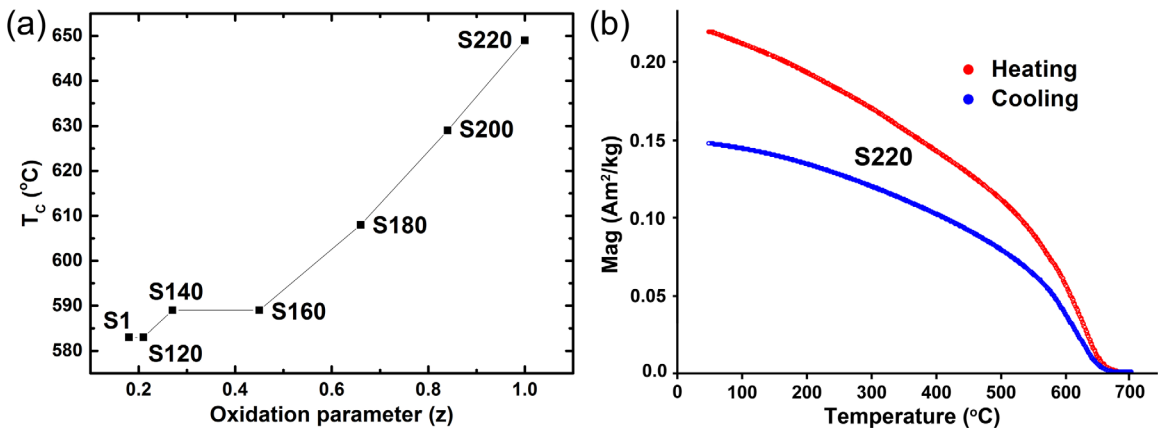

Figure 9. (a) Curie temperatures of Samples S1–S220 as a function of oxidation parameter z. (b) Thermomagnetic curve of Sample S220. Heating was performed in flowing helium in a field of 300 mT.

in coercivity that magnetoelastic effects due to induced stress contribute significantly to the resulting magnetic properties.

4.4. Implications for Paleomagnetic Studies

From the above observations, the reliability of the magnetic remanence of maghemitized rocks is called into question; the process of oxidation will lead to the acquisition of a new chemical remanent magnetizaton (CRM). Due to the shell growth mechanism, the original Fe_3O_4 phase in the core will effect the magnetic alignment of the γ-Fe_2O_3 shell [*Ge et al*., 2014]. It is likely that on average for a distribution of the particles the original magnetization direction will be retained. However, obtaining an paleointensity estimate may not be accurate for two reasons: (1) the core/shell CRM acquistion model may not always couple and the CRM of individiual particles may not be aligned with the orignal remanence and (2) whilst it might be theoretically possible to recover the paleointensity informaton from a γ-Fe_2O_3 sample, γ-Fe_2O_3 is generally unstable to heating, as evidenced by the thermomagnetic curve of Sample S220, and samples dominated by this phase are, therefore, likely to fail Thellier-type or other heating paleointensity protocols. It is also recognized that potential differences exist between these experimental results, which involve oxygen addition, compared to that undergone in mid-ocean ridges that may favor a Fe-removal mechanism for oxidation.

5. Conclusions

This study has investigated the maghemization of Fe_3O_4 grains in the PSD size range and the effect of this oxidation process on their magnetic properties. Complementary methods of XRD and Mossbauer spectroscopy followed this phase transformation as a function of temperature and showed the onset of oxidation was most pronounced at 160°C, with a reaction temperature of 220°C producing pure γ-Fe_2O_3. The phase transformation is confirmed by EELS analysis of the O *1s K*/Fe *2p* $L_{2,3}$ edges acquired from the precursor Fe_3O_4 grains and fully oxidized γ-Fe_2O_3 grains. High-resolution HAADF imaging and localized EELS analysis revealed evidence to suggest the surface to be more oxidized, supporting the formation of a core-shell Fe_3O_4/γ-Fe_2O_3 structure. Off-axis electron holography allowed for construction of magnetic induction maps of individual Fe_3O_4 and γ-Fe_2O_3 grains, revealing their PSD (vortex) nature in both cases, which is supported by corresponding first-order reversal curves characteristic of PSD states. Thermomagnetic curves showed an increase of T_C with reaction temperature that is consistent with maghemization process. The coercivity of the magnetite grains was shown to increase with reaction temperature up to 180°C, but decrease thereafter. This magnetic behavior is attributed to exchange coupling between a γ-Fe_2O_3 shell with the Fe_3O_4 core resulting in an energy minimum of SD state or a vortex state with reduced vorticity, with the latter considered the dominant mechanism in this study. Once fully oxidized to γ-Fe_2O_3, the domain states revert back to vortices with slightly reduced coercivity. It is suggested that heavily maghemized samples may not retain meaningful paleomagnetic signals.

Acknowledgments

The authors would like to thank the Natural Environment Research Council for funding (NERC grant NE/H00534X/1). Thanks also go to the Center for Electron Nanoscopy at the Technical University of Denmark for use of their microscopy facilities. The data for this paper are available at NERC-designated data center for the Earth sciences, the National Geoscience Data Centre.

References

Almeida, T. P., M. W. Fay, Y. Zhu, T. W. Hansen, R. E. Dunin-Borkowski, and P. D. Brown (2012), Environmental TEM investigation of the reduction of α-Fe_2O_3 nanorods under H_2 atmosphere, *J. Phys. Conf. Ser.*, *371*, 012049.

Almeida, T. P., T. Kasama, A. R. Muxworthy, W. Williams, L. Nagy, P. D. Brown, and R. E. Dunin-Borkowski (2014), Visualised effect of oxidation on magnetic recording fidelity in pseudo-single-domain magnetite particles, *Nat. Commun.*, *5*, 5154, doi:10.1038/ncomms6154.

Bleil, U., and N. Petersen (1983), Variation in magnetization intensity and low-temperature titanomagnetite oxidation of ocean floor basalts, *Nature*, *301*, 384–388.

Chen, J., D. J. Huang, A. Tanaka, C. F. Chang, S. C. Chung, W. B. Wu, and C. T. Chen (2004), Magnetic circular dichroism in Fe 2*p* resonant photoemission of magnetite, *Phys. Rev. B*, *69*, 085107.

Chen, S.-Y., A. Gloter, A. Zobelli, L. Wang, C.-H. Chen, and C. Colliex (2009), Electron energy loss spectroscopy and *ab initio* investigation of iron oxide nanomaterials grown by a hydrothermal process, *Phys. Rev. B*, *79*, 104,103.

Colliex, C., T. Manoubi, and C. Ortiz (1991), Electron-energy-loss-spectroscopy near-edge fine structures in the iron-oxygen system, *Phys. Rev. B*, *44*, 11,402–11,411.

Cornell, R. M., and U. Schwertmann (2003), *The Iron Oxides, Structure, Properties, Reactions, Occurrence and Uses*, pp. 664, John Wiley, Weinheim, Germany.

Crocombette, J. P., M. Pollak, F. Joliet, N. Thromat, and M. Gautier-Soyer (1995), X-ray-absorption spectroscopy at the Fe L2,3 threshold in iron oxides, *Phys. Rev. B*, *52*, 3143–3150.

Cullity, B. D., and S. R. Stock (2001), *Elements of X-ray Diffraction*, 3rd ed., Prentice Hall, N. J.

Da Costa, G. M., E. De Grave, P. M. A. De Bakker, and R. E. Vandenberghe (1995), Influence of nonstoichiometry and the presence of maghemite on the Mössbauer spectrum of magnetite, *Clays Clay Miner.*, *43*, 656–668.

Da Costa, G. M., C. Blanco-Andujar, E. De Grave, and Q. A. Pankhurst (2014), Magnetic nanoparticles for in vivo use: A critical assessment of their composition, *J. Phys. Chem. B*, *118*, 11,738–11,746.

Day, R., M. Fuller, and V. A. Schmidt (1977), Hysteresis properties of titanomagnetites: Grain size and composition dependence, *Phys. Earth Planet. Inter.*, *13*, 260–267.

Dunin-Borkowski, R. E., M. R. McCartney, and D. J. Smith (1998), Off-axis electron holography of magnetic materials, *Rec. Res. Dev. Appl. Phys.*, *1*, 119–131.

Dunlop, D. J. (2002), Theory and application of the Day plot (M_{rs}/M_s versus H_{cr}/H_c), 1. Theoretical curves and tests using titanomagnetite data, *J. Geophys. Res.*, *107*(B3), 2056, doi:10.1029/2001JB000486.

Dunlop, D. J., and Ö. Özdemir (2001), *Rock Magnetism: Fundamentals and Frontiers*, pp. 577, Cambridge Univ. Press, N. Y.

Fujii, T., F. M. F. De Groot, G. A. Sawatzky, F. C. Voogt, T. Hibma, and K. Okada (1999), In situ XPS analysis of various iron oxide films grown by NO_2-assisted molecular-beam epitaxy, *Phys. Rev. B*, *59*, 3195–3202.

Gallagher, K. J., W. Feitknecht, and U. Mannweiler (1968), Mechanism of oxidation of magnetite to γ-Fe_2O_3, *Nature*, *217*, 1118–1121.

Ge, K., W. Williams, Q. Liu, and Y. Yu (2014), Effects of the core-shell structure on the magnetic properties of partially oxidized magnetite grains: Experimental and micromagnetic investigations, *Geochem. Geophys. Geosyst.*, *15*, 2021–2038, doi:10.1002/2014GC005265.

Gloter, A., A. Douiri, M. Tence, and C. Colliex (2003), Improving energy resolution of EELS spectra: An alternative to the monochromator solution, *Ultramicroscopy*, *96*, 385.

Kasama, T., R. E. Dunin-Borkowski, and M. Beleggia (2011), Electron holography of magnetic materials, in *Holography–Different Fields of Application*, edited by F. A. M. Ramirez, pp. 53–80, InTech., Rijeka.

Krása, D., V. P. Shcherbakov, T. Kunzmann, and N. Petersen (2005), Self-reversal of remanent magnetization in basalts due to partially oxidized titanomagnetites, *Geophys. J. Int.*, *162*, 115–136.

Liu, Q. S., S. K. Banerjee, M. J. Jackson, C. L. Deng, Y. X. Pan, and R. X. Zhu (2004), New insights into partial oxidation model of magnetites and thermal alteration of magnetic mineralogy of the Chinese loess in air, *Geophys. J. Int.*, *158*, 506–514, doi:10.1111/j.1365-246X.2004.02348.x.

Mathew, D. S., and R.-S. Juang (2007), An overview of the structure and magnetism of spinel ferrite nanoparticles and their synthesis in microemulsions, *Chem. Eng. J.*, *129*, 51–65.

Matzka, J., D. Krása, T. Kunzmann, A. Schult, and N. Petersen (2003), Magnetic state of 10–40 Ma old ocean basalts and its implications for natural remanent magnetization, *Earth Planet. Sci. Lett.*, *206*, 541–553, doi:10.1016/s0012-821x(02)01094-4.

Muxworthy, A. R., and D. Dunlop (2002), First-order reversal curve (FORC) diagrams for pseudo-single-domain magnetites at high temperature, *Earth Planet. Sci. Lett.*, *203*, 369–382.

O'Reilly, W. (1984), *Rock and Mineral Magnetism*, 220 pp., Blackie Acad. and Prof, Glasgow, U. K.

Özdemir, Ö., and D. Dunlop (1988), Crystallization remanent magnetization during the transformation of maghemite to hematite, *J. Geophys. Res.*, *93*, 6530–6544.

Ramdani, A., J. Steinmetz, C. Gleitzer, J. M. D. Coey, and J. M. Friedt (1987), Perturbation de L'echange electronique rapide par les lacunes cationiques dans $Fe_{3-x}O_4$ ($x \leq 0{,}09$), *J. Phys. Chem. Solids*, *48*, 217–228.

Readman, P. W., and W. O'Reilly (1972), Magnetic Properties of Oxidized (Cation-Deficient) Titanomagnetites (Fe, Ti, □)$_3O_4$, *J. Geomagn. Geoelectr.*, *24*, 69–90.

Schmidbauer, E., and M. Keller (2006), Magnetic hysteresis properties, Mossbauer spectra and structural data of spherical 250 nm particles of solid solutions Fe_3O_4-gamma-Fe_2O_3, *J. Magn. Magn. Mater.*, *297*, 107–117.

Tauxe, L. (1998), *Paleomagnetic Principles and Practice*, Kluwer Acad., Dordrecht, Netherlands.

van Aken, P. A., and S. Lauterbach (2003), Strong magnetic linear dichroism in Fe L_{23} and O K electron energy-loss near-edge spectra of antiferromagnetic hematite α-Fe_2O_3, *Phys. Chem. Miner.*, *30*, 469.

Van Velzen, A. J., and J. D. A. Zijderveld (1995), Effects of weathering on single-domain magnetite in Early Pliocene marine marls, *Geophys. J. Int.*, *121*, 267–278.